applied sciences

MDPI

Article

High-Precision Numerical Research on Flow and Structure Noise of Underwater Vehicle

Hao Cao * and Lihua Wen

School of Astronautics, Northwestern Polytechnical University, Xi'an 710072, China
* Correspondence: caohao@163.com

Abstract: This paper presents the results of research on the noise generated by an underwater vehicle in the operational state. The study combines the large eddy simulated turbulence model and Lighthill's acoustic analogy theory and extracts the transient flow field data as the excitation conditions for acoustic calculations. The results of the numerical calculations of the external acoustic field were obtained under vehicle wall pressure pulsation condition, Lighthill volume excitation condition, and the vibration excitation condition of the underwater vehicle. It is found that the noise is concentrated at the front and tail of underwater vehicle, and its level is closely related to the form of vortex shedding. The peak frequency of structural radiation noise of underwater vehicle is consistent with its peak frequency of mean square vibration velocity. The basis for selecting the boundary conditions of the sound field according to the incoming flow conditions is also evaluated. The research results provide a reference for the noise reduction design of underwater vehicles, thus improving their concealment in combat.

Keywords: underwater vehicle; large eddy simulation; Lighthill's acoustic analogy; noise

Citation: Cao, H.; Wen, L. High-Precision Numerical Research on Flow and Structure Noise of Underwater Vehicle. *Appl. Sci.* **2022**, *12*, 12723. https://doi.org/10.3390/app122412723

Academic Editors: Lin Mu, Enjin Zhao and Hao Qin

Received: 14 November 2022
Accepted: 5 December 2022
Published: 12 December 2022

1. Introduction

Torpedoes, submarines, and other underwater vehicles are the main combat tools of national navies and play an important role in assault operations, striking military targets, and reconnaissance owing to their high navigation speed, long range, and stealth. However, in the context of rapid development of soft and hard kill technologies such as sonar technology to combat underwater high-speed vehicles, how to improve the survivability of underwater vehicles has become a key technology in the military field. Underwater vehicles inevitably generate noise during their missions, and for every 5 dB increase in noise, the probability of hitting a target is reduced by 25%, thus directly affecting their stealth and deterrence. Therefore, underwater high-speed vehicles with silent characteristics have received much attention from various navies. The underwater noise is mainly generated by the pulsating pressure on the surface of vehicle and the disturbance within the turbulent boundary layer around the surface, and it is difficult to reduce the noise using general methods. Therefore, it is important to study the mechanism of underwater vehicle noise generation to improve its concealment.

The study of noise begins with a focus on turbulence and pulsating pressure, which was usually studied by theoretical analysis and experimental verification. However, theoretical analysis is only applicable to a simplified model, which cannot describe the phenomenon of a complex flow; experimental verification is also not widely used because of its high cost, long cycle time, and small measurement range. With the development of computer technology and improvement of computer performance, computational fluid dynamics (CFD) has become an important tool for solving flow problems. After the SUBOFF submarine model was proposed in the United States in 1989 and a series of experimental data were obtained, many numerical simulation studies based on this model and data were also carried out [1]. Alin analyzed a fully attached SUBOFF flow field variation using

Unsteady Reynolds Averaged Navier Stokes (URANS) [2], Detached Eddy Simulation (DES), and Large Eddy Simulation (LES) [3], discussed the accuracy of different numerical computational models, and finally found the advantages of DES and LES for solving the pulsation-related terms. Bensow [4] and Holloway [5] analyzed the viscous flow field and flow-separation phenomena in SUBOFF submarines using LES and verified the accuracy of LES in flow field simulations when compared with experimental values. Kim and Sung [6] directly used Direct Numerical Simulation (DNS) to calculate the pulsation pressure within the boundary layer of a two-dimensional model flow field. However, DNS is poorly applicable because of the high requirements of computer hardware. Therefore, to balance the computational resources and solution accuracy, it is gradually becoming a research trend to use LES to obtain turbulent flow field data.

After separating the acoustic terms from the equations using the acoustic analogy theory proposed by Lighthill [7,8], the flow field calculations were successfully combined with the acoustic field calculations and numerical calculations on developing noise. Wang et al. [9] simulated the complex flow field of a submarine with a propeller based on LES and analyzed the sound pressure spectrum and noise-pointing characteristics of the submarine using ACTRAN software. It was found that the noise of the submarine with a propeller was concentrated in the low-frequency band, and the high-pressure region of the propeller contributed the most to the noise. Piomelli et al. [10] studied the effect of small-scale eddies on noise and found that the low-frequency part of the noise was better solved using the LES turbulence model. Both Bailly [11] and Moon [12] studied flat plate noise. Bailly [11] used the acoustic analogy method to study flat plates subjected to pulsating pressure and verified the feasibility of the acoustic analogy method by comparing the data with direct acoustic field calculations. Moon [12] studied the sound pressures of flat plates under different operating conditions based on a combination of LES and linearized perturbed compressible equations (LPCE), and found that the numerical calculation results are consistent with the experimental data. Lighthill's acoustic analogy theory can guarantee the accuracy of calculation, and a combination of high-precision numerical simulation with the theory is widely used in the field of noise solution.

In this study, we first obtained the data of velocity pulsation and pressure pulsation of a type of underwater vehicle by conducting a numerical simulation of flow field with high accuracy using LES. These pulsation data are then used as the excitation for the subsequent noise calculation, and finally the noise radiation characteristics and acoustic vibration coupling phenomenon of this underwater vehicle are determined. The first part of the article presents the theory involved in the numerical solution and the modeling of flow field and acoustic field. The Section 1 of the second part shows the results of numerical calculations of external flow field of underwater vehicle. The second part of the Section 2 analyzes the results of numerical calculations of external sound field of underwater vehicle under two boundary conditions: vehicle wall pressure pulsation condition and Lighthill volume excitation condition. The Section 3 of the second part considers the material and structural properties of underwater vehicle and analyzes its structural radiation noise. Finally, the study is summarized, and future research directions are given.

2. Theory And Model Building

2.1. Large Eddy Simulation

LES uses the N-S equation to directly model large-scale vortices. The equations for large-scale vortex control are obtained by filtering vortices that are smaller than the filter width or grid size using the filtering process.

The filtering function can be expressed as follows:

$$G(x, x') = \begin{cases} 1/V, x' \in V \\ 0, x' \notin V \end{cases} \quad (1)$$

where V is the control volume.

The filtered equation is given by:

$$\frac{\partial \rho}{\partial t} + \frac{\partial}{\partial x_i}(\rho \overline{u_i}) = 0 \tag{2}$$

$$\frac{\partial}{\partial t}(\rho \overline{u_i}) + \frac{\partial}{\partial x_j}(\rho \overline{u_i u_j}) = \frac{\partial}{\partial x_j}(\sigma_{ij}) - \frac{\partial \overline{p}}{\partial x_i} - \frac{\partial \tau_{ij}}{\partial x_j} \tag{3}$$

where ρ is the fluid density; t is the time; p is the pressure; σ_{ij} is the stress tensor due to molecular viscosity; τ_{ij} is the sublattice scale stress.

2.2. Lighthill's Acoustic Analogy Theory

The Lighthill acoustic analogy theory approximates the complex sound source formed by fluid motion as a static medium equivalent source to solve difficult problems to accurately describe the sound source. The theory assumes that the coupling between the fluid and sound field exists only in the near field, and considers the far field as the acoustic radiation region, whose flow has almost no effect on the sound field, where $\rho_a = \rho - \rho_0$, $P_a = P - P_0$, ρ_0 and P_0 represents the density and sound pressure. Then, the equation can be expressed as follows:

$$\frac{\partial^2 \rho_a}{\partial t^2} - c_0^2 \frac{\partial^2 \rho_a}{\partial x_i x_j} = \frac{\partial^2 T_{ij}}{\partial x_i x_j} \tag{4}$$

$$T_{ij} = \rho v_i v_j + \delta_{ij}\left[(P - P_0) - c^2\left(\rho - \rho^2\right)\right] - \tau_{ij} \tag{5}$$

where c_0 is the velocity of sound under isentropic conditions; T_{ij} is the Lighthill stress tensor; δ_{ij} is the elastic constant; τ_{ij} is the viscous stress.

As the viscous stress is a small amount of Reynolds stress and can be neglected, the final equation can be simplified as follows:

$$\frac{\partial^2 \rho_a}{\partial t^2} - c_0^2 \frac{\partial^2 \rho_a}{\partial x_i x_j} = \frac{\partial^2 T_{ij}}{\partial x_i x_j} \tag{6}$$

$$T_{ij} = \rho_0 v_i v_j \tag{7}$$

This equation is the basic equation of Lighthill's acoustic analog theory, which can be solved for turbulent pulsating pressure direct radiation noise.

2.3. Model Building

Figure 1a shows the underwater vehicle studied in this paper, which is a standard rotary body of 3.29 m in length. Figure 1b shows the computational domain of cylindrical flow field created from the model shape. The length of the front end part is taken as the length of the underwater vehicle. To accurately capture the trailing vortex region at the trailing edge of underwater vehicle, the trailing end is taken as twice the length of underwater vehicle. The diameter of computational domain is taken as 4.45 m. FLUENT MESHING was used for meshing, and the y^+ value was taken as 1. To accurately capture the vortex region that may be generated by the flow and the region with large parameter variations, the cylindrical region and tail section that wraps the whole underwater vehicle are locally encrypted. The final total number of generated meshes is about 27 million.

To facilitate the observation and analysis of sound field radiation characteristics and to avoid the effect of geometric features such as the sharp corners of calculation domain on sound field radiation, the acoustic field calculation domain was selected as the spherical region shown in Figure 1c. The diameter of the sphere was taken as three times the length of underwater vehicle. The noise in the low-frequency band (below 2000 Hz) was calculated using ACTRAN. According to the required calculation frequency, the accuracy of acoustic calculation results can be ensured when each wavelength contains at least six acoustic grids,

so the maximum size of acoustic grid is set to 0.12 m. ICEM was used to divide the grid, and the total number of grids is about 6 million.

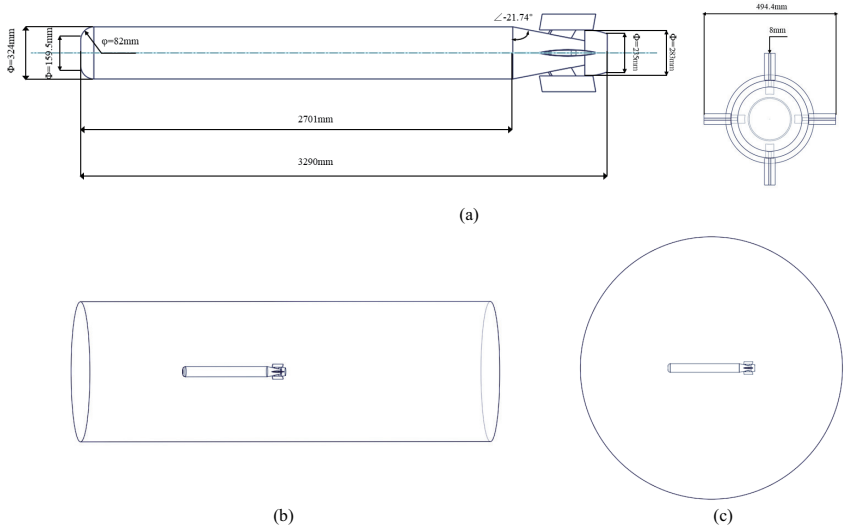

Figure 1. Diagram of the model. (**a**) Underwater vehicle model (**b**) Flow field calculation domain (**c**) Acoustic computational domain.

To detect the flow field and acoustic field of underwater vehicle, 14 monitoring points were set up at the front and tail of underwater vehicle. The distance of each monitoring point from the wall is 1 m, as shown in Figure 2.

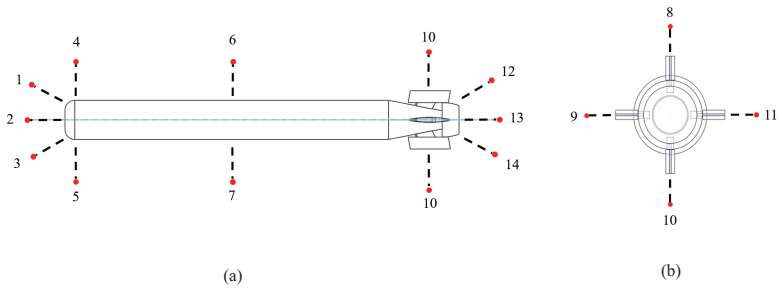

Figure 2. Monitoring point location diagram. (**a**) Side view (**b**) Rear view.

3. Results And Discussion

3.1. Calaulation Results of Flow Field

The study set the entrance boundary condition as the velocity entrance. The velocity was taken as a torpedo navigation speed of 19 m/s. The torpedo wall was set as no-slip condition, and the outer field boundary was set as no-shear condition. To provide a better initial field for the transient calculation to converge and stabilize faster, the standard k–e model was first selected for steady-state calculation. In the steady-state calculation section, the broadband noise source model was turned on to perform a preliminary estimation and analysis of the entire fluid domain sound field. The results are shown in Figure 3a.

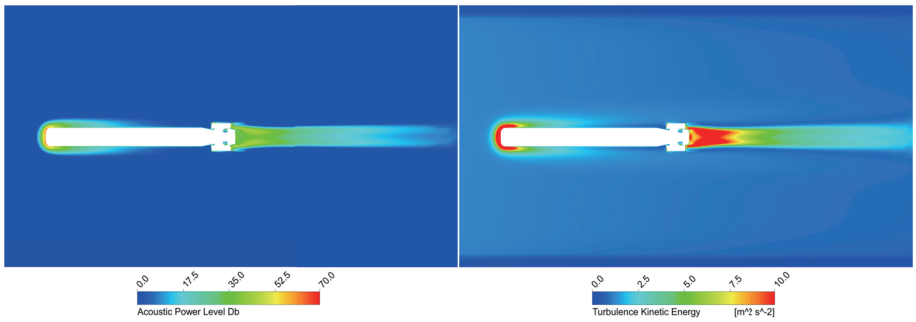

(a) (b)

Figure 3. Steady-state calculation results. (**a**) Distribution of sound power level (**b**) Distribution of turbulent kinetic energy.

The accuracy of noise data obtained from the broadband noise source model simulation is not high because it uses a constant Reynolds averaging model to calculate the noise. However, this model has a natural advantage in quickly determining the location of noise source. The sound power level diagram shows that the noise source is mainly concentrated in the torpedo head and wake vortex area behind the torpedo tail. A comparison with the turbulent kinetic energy shows that the noise generation region highly overlaps with the turbulence concentration region, and it can be assumed that the noise mainly originates from the turbulence region.

Based on the results of steady-state calculations, an LES with a Smagorinsky–Lilly subgrid scale model was used to carry out the transient solution process, and the calculation time step was set to 1×10^{-5} s according to the grid size and acoustic conditions. The Q criterion was used to describe the vortex structure of transient flow field, as shown in Figure 4. It was found that the vortex structure is concentrated at the rear of the torpedo blade, which corresponds to the abovementioned sound power level distribution and turbulent kinetic energy distribution, indicating that the vortex structure is closely related to the generation of flow noise and is the cause of flow noise.

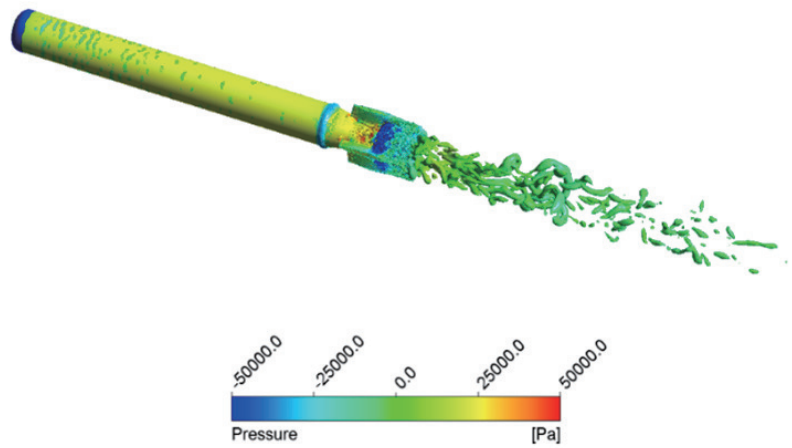

Figure 4. Vortex structure.

3.2. Calculation Results of Flow Noise

According to the acoustic solution theory, sound sources can be divided into three types: monopole, dipole, and quadrupole sources. In the flow field radiation noise, the noise caused by turbulent phenomena such as boundary layer and vortex development in the flow field is a quadrupole noise source, and the vehicle wall pressure pulsation caused by turbulent activity is a dipole noise source. Monopole and dipole noises are surface sources, whereas quadrupole noise is a volume source. Some studies reported that when the flow velocity is low, the surface–source noise can be mainly considered,

and the volume–source noise is neglected. Therefore, most researchers do not consider the quadrupole source when solving and directly use the vehicle wall pulsation pressure as the source excitation for calculation. However, the underwater vehicle is faster. The quadrupole noise ratio may increase in this case, and the flow field results calculated in the previous section may improve. The underwater vehicle has a large wake vortex area, which is filled with large and small vortices, and its generation, development, and breaking inevitably generate noise. Therefore, it can be inferred that the noise calculation in this region cannot ignore the influence of quadrupole noise source generated by the vortex motion. A comparative analysis of the study was performed using wall pulsation pressure and Lighthill volume sound source as the excitation for acoustic calculations. For all the results reported in this paper, the reference sound pressure is taken as 1×10^{-6} Pa.

3.2.1. Calculation Results for Pulsating Pressure Excition

In the case where the pulsating pressure on wall is used as the excitation, the vehicle wall pressure pulsation is extracted from the flow field data and used as a boundary condition for further calculation. The extracted wall pressure pulsation at some frequencies is shown in Figure 5, and the unit was set to dB.

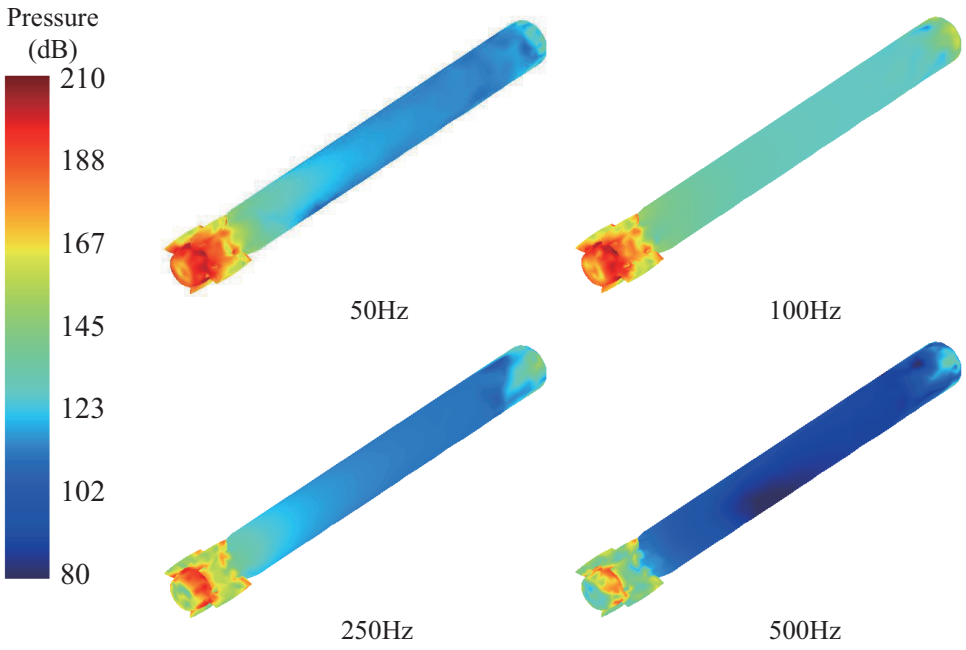

Figure 5. Pulsating pressure on the vehicle wall.

Figure 5 shows that the pulsating pressure distribution on the wall of underwater vehicle is inextricably related to the distribution of vortex region of flow field, and there is a high pulsating pressure distribution in the vortex-dense area of both the leading and trailing edges of underwater vehicle, more obvious at the trailing edge. It is easy to observe that the pulsating pressure on the vehicle wall is higher in the low-frequency part and lower in the high-frequency part. For the same frequency, the underwater vehicle has a large pulsating pressure area in the wake region, which is caused by the wake vortex area. Below 500 Hz, as the frequency increases, the large pulsating pressure region in the tail gradually decreases, and by around 500 Hz, it decreases to a very small portion and does not change much until higher frequencies are applied. Large vortices have a greater impact on the low-frequency noise situation, while small vortices affect the high-frequency noise results. A comparison of the vortex structure diagram of transient flow field can lead to the conclusion that large vortices play a major role in generating the pulsating pressure on the vehicle wall.

Figure 6a shows the calculation results of sound pressure at monitoring points 1, 2, and 3. It can be observed that the spectral characteristics of sound pressure levels at these monitoring points are very similar, although monitoring point 2 is located above the axis, while monitoring points 1 and 3 are symmetrically distributed on both sides of the axis. This indicates that the acoustic radiation distribution at the front of the underwater vehicle is approximately the same in all the directions. This can be explained by the absence of substantial vortex and turbulence properties in the front, which would not produce a large source of stream noise. In addition, the amplitude and trend of the frequency domain distribution curves of sound pressure at symmetric monitoring points (e.g., receivers 6 and 7 and receivers 8–11) are almost the same, although there is a certain directionality at the corresponding frequency values.

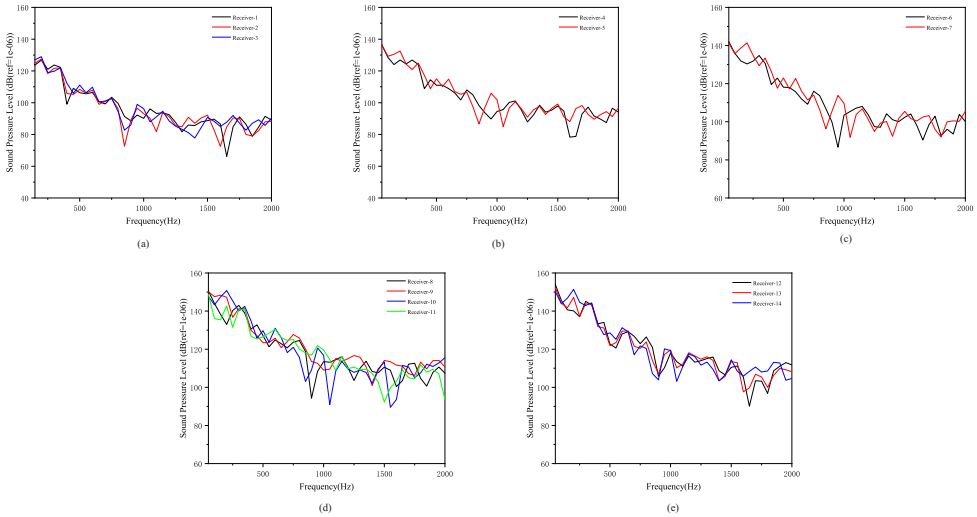

Figure 6. Spectral characteristics of sound pressure at different monitoring points along the flow direction considering pressure pulsation excitation. (**a**) Receiver 1–3 (**b**) Receiver 4–6 (**c**) Receiver 6–7 (**d**) Receiver 8–11 (**e**) Receiver 12–14.

Several representative monitoring points were selected to compare the changes in sound pressure levels along the flow direction, as shown in Figure 6. In the case where the pulsating pressure is the excitation, the sound pressure level substantially varies along the flow direction, with the highest value of about 135 dB in the low-frequency part and also around 90 dB in the high-frequency part at several monitoring points (receivers 1–5) at the front of underwater vehicle. By the middle of the underwater vehicle (receivers 6 and 7), the sound pressure level improved considerably, probably by about 6 dB, and in the whole tail section of underwater vehicle and the subsequent part of the area (receivers 8–14), the sound pressure level increased integrally by about 8 dB. The highest value of low-frequency part in this region is about 150 dB, whereas the high-frequency part is also about 110 dB.

The sound pressure distribution diagram of the middle section of underwater vehicle can show the sound field radiation more clearly, as shown in Figure 7. The sound pressure level shows a general trend of gradually decreasing with increasing frequency, but a small increase in sound pressure level might have occurred at some frequencies. The highest values of sound pressure levels appear around the blades in the wake of torpedo, which is due to the complex shape of blades and the tendency to obtain stronger disturbances in the flow. The change in sound pressure along the radius direction does not always decrease, indicating the oscillatory nature of sound waves.

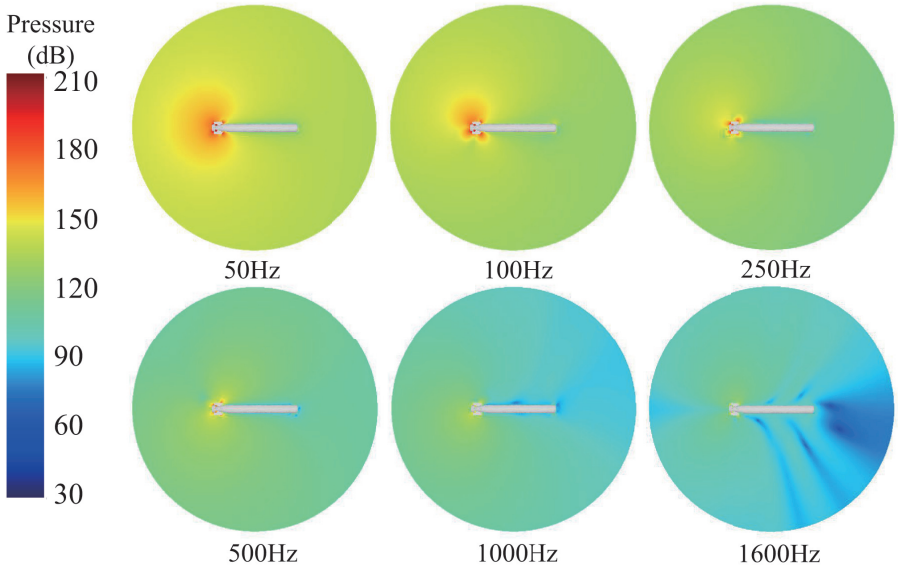

Figure 7. Sound pressure level distribution for pressure pulsation excitation.

3.2.2. Calculation Results for Lighthill Volume Excition

The calculation results for the Lighthill volume as an acoustic excitation are shown in Figure 8, and a comparison of the calculation results regarding Lighthill and pulsating pressure is shown in Figure 9. Except for monitoring point 13 in the tail vortex area, the comparisons of the rest (monitoring points 1–12 and 14) are not very different, and they all show a greater sound pressure level of the calculation results from the pulsating pressure as the excitation. Therefore, only the cases of monitoring points 1 and 13 are shown in Figure 9. When the difference in sound pressure level is 20 dB, the difference in sound pressure is at least one order of magnitude (as Equation (8)), so it is reasonable for researchers to ignore quadrupole sources in fluid-radiated noise calculations and consider pulsating pressure alone as a dipole source, slightly affecting the calculation results.

$$L = 20 \lg \frac{p}{p_{ref}} \tag{8}$$

where L is the sound pressure level; p is the sound pressure; p_{ref} is the reference sound pressure, taken as 1×10^{-6} Pa.

In one case at monitoring point 13, the calculated sound pressure level for Lighthill volume excitation within 200 Hz is substantially higher than the calculation results for pulsating pressure excitation, verifying our assumption that the quadrupole source has non-negligibility in some regions due to very intense vortex activity at a higher velocity flow. Of course, for most applications, appropriate neglect can simplify the calculation process and provide acceptable results.

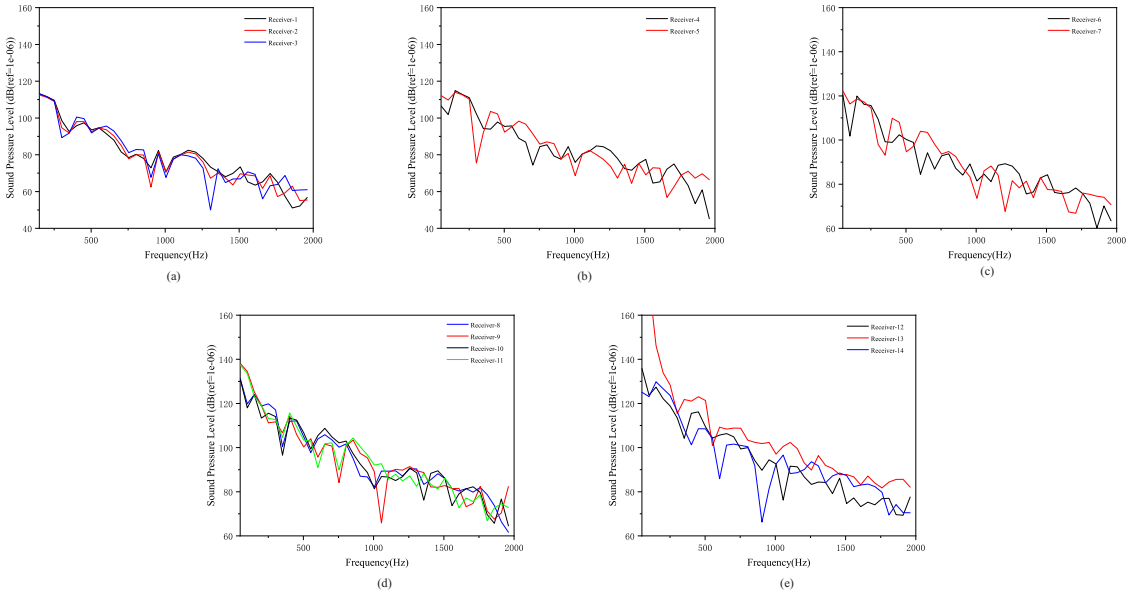

Figure 8. Spectral characteristics of sound pressure at different monitoring points along the flow direction considering Lighthill volume excition. (**a**) Receiver 1–3 (**b**) Receiver 4–6 (**c**) Receiver 6–7 (**d**) Receiver 8–11 (**e**) Receiver 12–14.

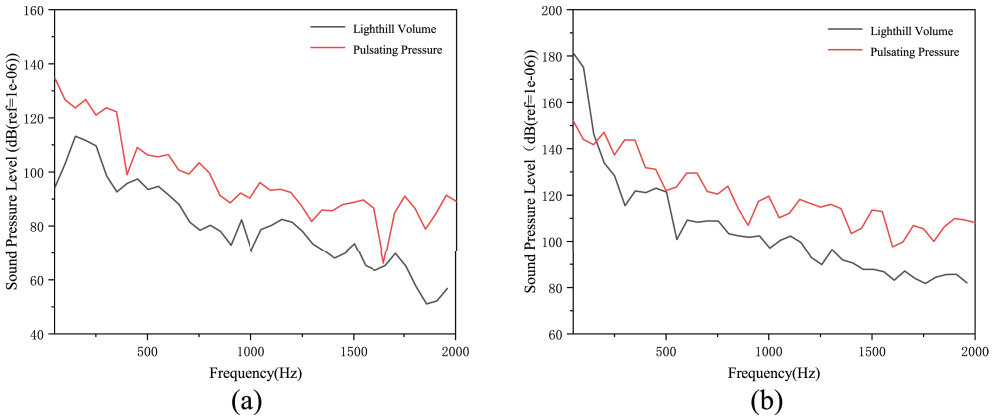

Figure 9. Comparison results of spectral characteristics. (**a**) Receiver 1 (**b**) Receiver 13.

3.3. Coupling Calculation and Structural Radiation Noise Analysis

To fully characterize the radiated noise of underwater vehicle, the relevant structure-radiated noise calculations were also carried out. In structure-radiated noise calculations, the structure is considered as an elastomer, which deforms and vibrates under the pulsating pressure at the vehicle wall and acts as a radiated noise source. Therefore, the structural mesh is imported, and the pulsating pressure is applied to the solid surface for coupled calculations. When the deformation of the surface of structure is small, the changes in flow field caused by the deformation of structure are negligible. Therefore, only the action of the fluid on the solid can be considered to simplify the calculation process, while ensuring the accuracy and precision of the calculation.

In this section, the results of flow field calculations are used as input boundary conditions for subsequent related calculations, and the computational domain is still taken as a spherical region of the same size. To simulate the shell vibration of a realistic underwater vehicle, the interior of underwater vehicle shown in Figure 1a was selectively hollowed out with a shell thickness of 20 mm. The material is set to Aluminum alloy with a Young's modulus of 8.2×10^{10} N/m^2, Poisson's ratio of 0.33, and density of 2820 kg/m^3, and its intersection was set to the coupling surface.

Using the vehicle wall pressure pulsation data as a boundary condition, coupled calculations were carried out to obtain the vibration displacement of underwater vehicle, as shown in Figure 10. The results show that under the effect of wall pulsation pressure, the vibration displacements throughout the solid domain are similar to the wall pressure pulsation distribution, both showing a trend towards larger values in the low-frequency part and smaller values in the high-frequency part. At 50 Hz, the underwater vehicle's stern section reached a maximum vibration displacement of the order of 10^{-5} m, while the high-frequency section is much less than this. For example, the maximum vibration displacement of a 750 Hz torpedo is only in the order of 10^{-9} m. It is precise because the low-frequency part of vibration is more intense, and the large eddies can be considered to play a crucial role while generating the vibration.

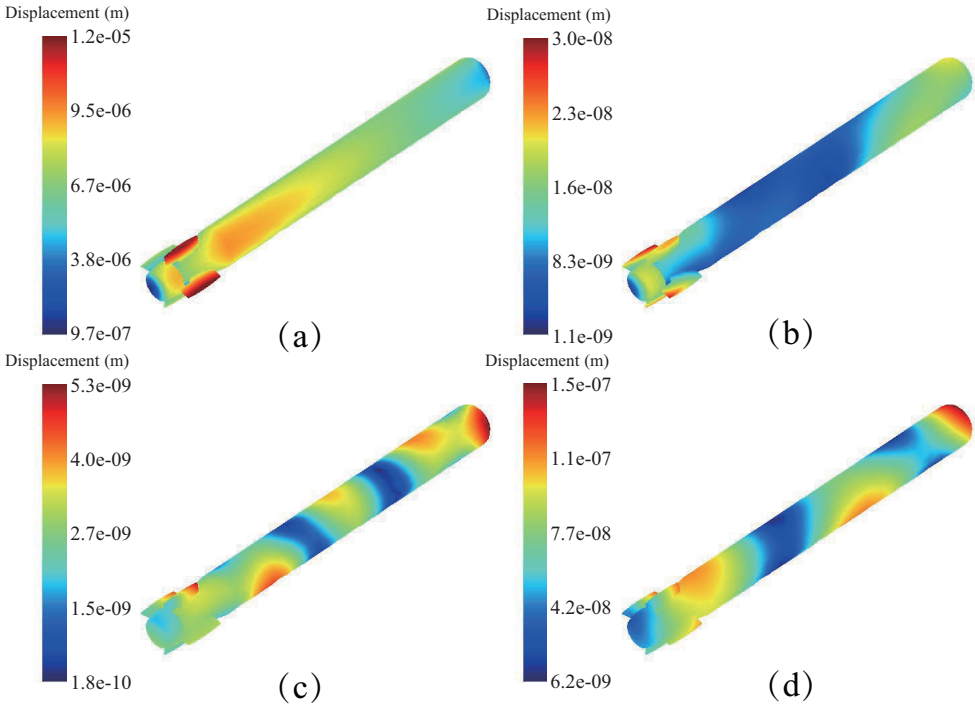

Figure 10. (**a**–**d**) Vibration displacement distribution.

The mean square vibration speed characteristics of underwater vehicle were obtained, as shown in Figure 11. In general, the mean square speed decreases as the frequency increases, i.e., the mean square speed is generally higher in the low-frequency part than in the high-frequency band. The results of other researchers show that the location of peak frequency point is only related to the structural model itself and is not related to the strength of flow excitation vibration at different flow velocities. Therefore, it can be assumed that the larger peak vibration velocity points for this structural underwater vehicle are located roughly at the frequency points of 300 Hz, 850 Hz, 1400 Hz, and 1850 Hz.

The frequency domain distribution curve of the structure's radiated noise shows distinctly different characteristics from the flow field radiated noise, showing a more pronounced vibration profile.

Several representative monitoring points were selected to show the frequency domain curves of sound pressure levels at their locations, as shown in Figure 12. It can be observed that whether the monitoring point is located at the leading, middle, or trailing edge of underwater vehicle, the structure-radiated noise has several corresponding peaks, all corresponding to the same frequency and peak frequency corresponding to the mean square vibration speed characteristic of torpedo. It can be inferred that this characteristic is related to the structure of underwater vehicle, and it is an inherent characteristic. From the sound pressure level curves of each monitoring point, it can be observed that the structure-

radiated noise is not very much related to distribution along the flow direction. Most of the monitoring points have the same trend and amplitude. In the low-frequency part, most of them are located around 125 dB, and the main peak points are located around 130 dB. Compared to the central part of underwater vehicle (receivers 4–7), the sound pressure levels at the leading edge of underwater vehicle (receivers 1–3) are in contrast larger than those at the trailing edge, which is an important feature that clearly differs from the fluid-radiated noise. In the high-frequency part, the sound pressure levels are also around 100 dB. In addition, monitoring point 13 has consistently higher sound pressure levels in fluid-radiated noise and lower values in structure-radiated noise, indicating that structure-radiated noise is very different from fluid-radiated noise in terms of propagation direction.

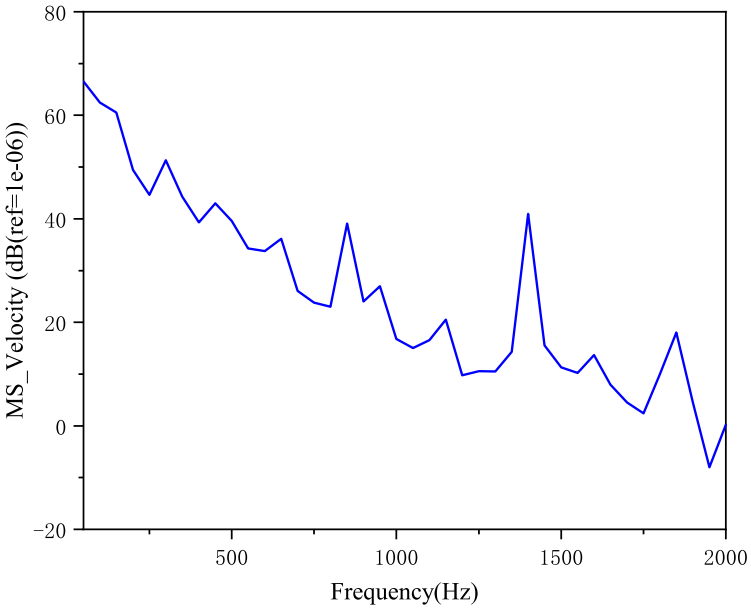

Figure 11. Mean square vibration characteristics.

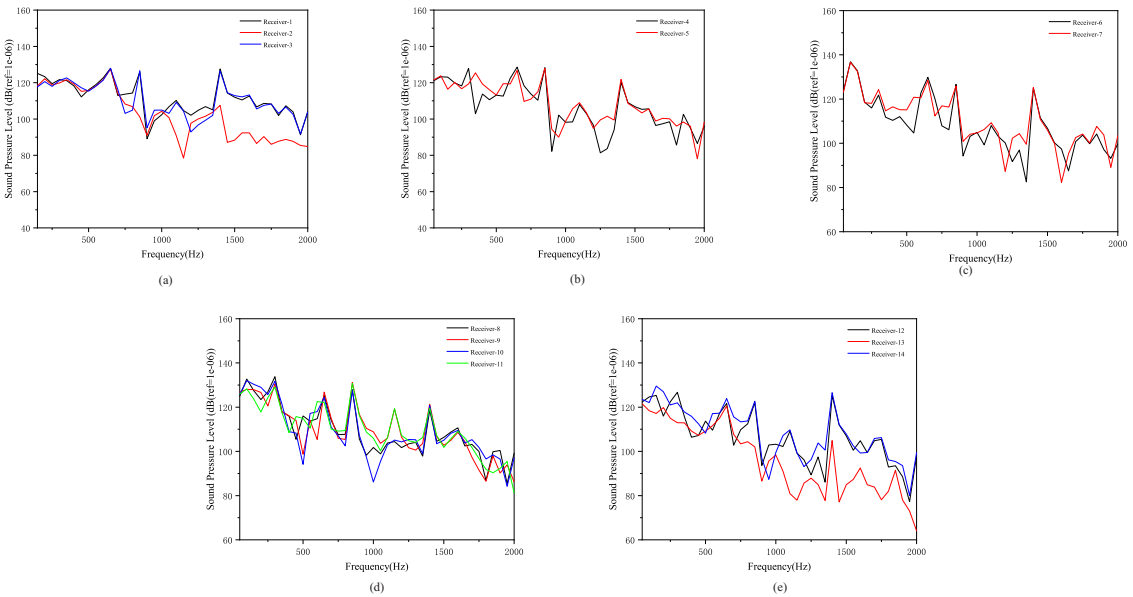

Figure 12. Spectral characteristics of sound pressure at different monitoring points along the flow direction considering vibration excitation. (**a**) Receiver 1–3 (**b**) Receiver 4–6 (**c**) Receiver 6–7 (**d**) Receiver 8–11 (**e**) Receiver 12–14.

For Monitoring Points 1, 2, and 3, the sound pressure level frequency domain distribution curves are shown in Figure 12a. Apart from the obvious peak in the curve, the sound pressure levels at monitoring point 2 are substantially different from the other two monitoring points. After the peak sound pressure level point at 1400 Hz, the sound pressure level in the high-frequency part of monitoring point 2 decreased below 90 dB, while the sound pressure level of the other two monitoring points remained at around 100 dB. After comparing the curves of monitoring points in the trailing edge section (shown in Figure 12e), it is demonstrated that the structure radiates less noise in the direction of axis of the underwater vehicle, which is particularly noticeable at high frequencies.

To facilitate further analysis of radiation characteristics of sound field, a cloud of sound pressure levels for structure-radiated noise generated by structural vibration due to pulsating pressure at the vehicle wall is given in Figure 13. It can be observed that the pulsating sound pressure cloud at 100 Hz is a left-right symmetrical pattern, which is due to the axisymmetrical shape of underwater vehicle, i.e., the low-frequency band has a stronger acoustic directivity at the head and tail, but the blade section radiates more widely, indicating that the tail is more directive than the head of underwater vehicle. Above 100 Hz, the sound field gradually becomes more "flap-like", and the flap-like features become more pronounced as the frequency increases. When the frequency reaches 2000 Hz, the "flap-like" distribution is already very dense. As the frequency increases further, the "flap-like" features gradually develop to the left and right, and this flap-like feature, which characterizes the fluctuation and oscillation of sound pressure, often leads to a lower sound pressure level region in the direction of underwater vehicle axis.

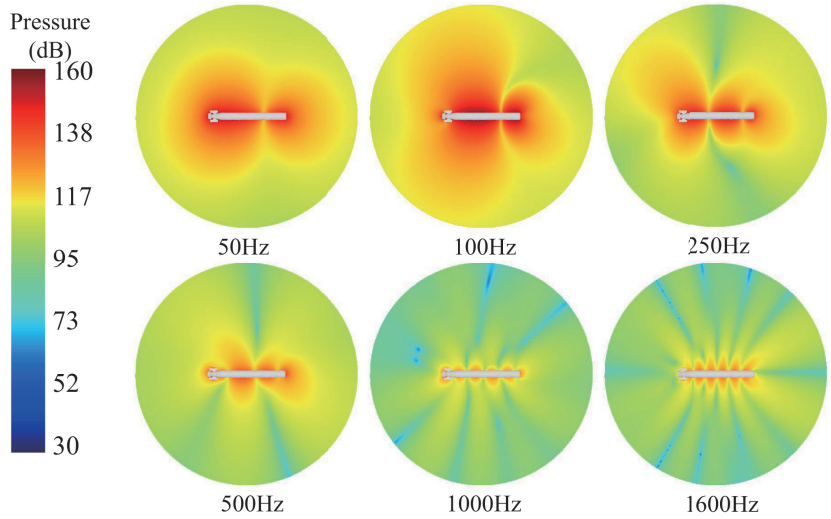

Figure 13. Sound pressure level distribution of structure-radiated noise at specific frequencies.

4. Conclusions

To improve the survivability and effective strike capability of underwater vehicles, this study used various approaches to simulate the radiation characteristics of their sound fields. This study mainly focuses on fluid-radiated noise and structure-radiated noise, and some necessary comparisons and analyses were made.

The head and tail of an underwater vehicle are the main sources of fluid-radiated noise, especially in the trailing vortex region of trailing edge section. Pressure pulsations generated by transient characteristics as well as the formation, development, and breaking of the vortex itself are relatively important sources of noise. In most cases, it is reasonable to ignore the quadrupole source such as volume excitation and consider only the wall pulsation pressure as the dipole source for excitation. However, in the case under the conditions of this study, ignoring the quadrupole source may have a bad effect, which needs to be considered and traded off in some practical applications.

The frequency domain distribution curve of structure-radiated noise is very different from that of fluid-radiated noise. In the high frequency part, peaks in the sound pressure levels occur, and these peaks are not lower than those in the low-frequency part. The peaks appear at approximately the same frequency at each monitoring point, which is related to the structure of underwater vehicle and is an inherent characteristic of the underwater vehicle. The sound pressure level diagram of structure-radiated noise is also very different from that of fluid-radiated noise, which shows obvious flap-like distribution characteristics at higher frequencies, and the number of flaps increases with frequency and gradually develops to both sides of the torpedo. The sound pressure level of the high-frequency part in the direction of torpedo axis is relatively low, corresponding to the frequency domain distribution curve. For the conditions studied in this paper, the structure-radiated noise and fluid-radiated noise have the same order of magnitude and do not differ much.

In the future, we will carry out multiconditions and multimorphology underwater vehicle flow field and sound field calculation, and explore a more universal trend from changing the flow velocity and changing the model, to provide guidance to general underwater vehicle researchers for model design and noise reduction design.

Author Contributions: Conceptualization, H.C.; Software, H.C.; Writing—original draft, H.C.; Writing—review & editing, H.C.; Supervision, L.W. All authors have read and agreed to the published version of the manuscript.

Funding: This research received no external funding.

Institutional Review Board Statement: Not applicable.

Informed Consent Statement: Not applicable.

Data Availability Statement: The data that support the findings of this study are available from the corresponding author upon reasonable request.

Conflicts of Interest: The authors have no conflicts to disclose.

References

1. Groves, N.C.; Huang, T.T.; Chang, M.S. *Geometric Characteristics of DARPA (Defense Advanced Research Projects Agency) SUBOFF Models (DTRC Model Numbers 5470 and 5471)*; Technical Report; David Taylor Research Center Bethesda MD Ship Hydromechanics Dept: Belhesda, MD, USA , 1989.
2. Alin, N.; Fureby, C.; Svennberg, S.; Sandberg, W.; Ramamurti, R.; Wikstrom, N.; Bensow, R.; Persson, T. 3D unsteady computations for submarine-like bodies. In Proceedings of the 43rd AIAA Aerospace Sciences Meeting and Exhibit, Reno, NV, USA, 10–13 January 2005; p. 1104.
3. Alin, N.; Bensow, R.; Fureby, C.; Huuva, T.; Svennberg, U. Current capabilities of DES and LES for submarines at straight course. *J. Ship Res.* **2010**, *54*, 184–196. [CrossRef]
4. Bensow, R.; Persson, T.; Fureby, C.; Svennberg, U.; Alin, N. Large eddy simulation of the viscous flow around submarine hulls. In Proceedings of the 25th ONR Symposium on Naval Hydrodynamics, St. Johns, NL, Canada, 8–13 August 2004.
5. Holloway, A.; Jeans, T.; Watt, G. Flow separation from submarine shaped bodies of revolution in steady turning. *Ocean Eng.* **2015**, *108*, 426–438. [CrossRef]
6. Kim, J.; Sung, H.J. Wall pressure fluctuations and flow-induced noise in a turbulent boundary layer over a bump. *J. Fluid Mech.* **2006**, *558*, 79–102. [CrossRef]
7. Lighthill, M.J. On sound generated aerodynamically I. General theory. *Proc. R. Soc. Lond. Ser. A Math. Phys. Sci.* **1952**, *211*, 564–587.
8. Lighthill, M.J. On sound generated aerodynamically II. Turbulence as a source of sound. *Proc. R. Soc. Lond. Ser. A Math. Phys. Sci.* **1954**, *222*, 1–32.
9. Wang, S.; Tang, J.; Wang, W.; Zhang, X. Numerical prediction of propeller excitation force and hydrodynamic noise of submarine with propeller. *Chin. Ship Res.* **2019**, *14*, 43–51.
10. Piomelli, U.; Streett, C.L.; Sarkar, S. On the computation of sound by large-eddy simulations. *J. Eng. Math.* **1997**, *32*, 217–236. [CrossRef]
11. Bailly, C.; Bogey, C.; Gloerfelt, X. Some useful hybrid approaches for predicting aerodynamic noise. *Comptes Rendus Mec.* **2005**, *333*, 666–675. [CrossRef]
12. Moon, Y.; Seo, J.; Bae, Y.; Roger, M.; Becker, S. A hybrid prediction method for low-subsonic turbulent flow noise. *Comput. Fluids* **2010**, *39*, 1125–1135. [CrossRef]